Blocking and Frontogenesis by Two-Dimensional Terrain in Baroclinic Flow. Part I: Numerical Experiments

Stephen T. Garner

NOAA/Geophysical Fluid Dynamics Laboratory, Princeton, New Jersey

ABSTRACT

The shallow atmospheric fronts that develop in the early winter along the east coast of North America have been attributed, in various modeling and observational studies, to the land–sea contrasts in both surface heating and friction. However, typical synoptic conditions are such that these ''coastal'' fronts could also be a type of upstream influence by the Appalachian Mountain chain. Generalized models have suggested that relatively cold air can become trapped on the windward side of a mountain range during episodes of warm advection without a local contribution from differential surface fluxes. Such a process was proposed decades ago in a study of observations along the coast of Norway. Could coastal frontogenesis be primarily a consequence of a mountain circulation acting on the large-scale temperature gradient?

A two-dimensional, terrain-following numerical model is used to find conditions under which orography may be sufficient to cause blocking and upstream frontogenesis in a baroclinic environment. The idealized basic flow is taken to have constant vertical shear parallel to a topographic ridge and a constant perpendicular wind that advects warm or cold temperatures toward the ridge. Land–sea contrasts are omitted. In the observed cases, the mountain is ''narrow'' in the sense that the Rossby number is large. This by itself increases the barrier effect, but the experiments show that large-scale warm advection is still crucial for blocking. For realistic choices of ambient static stability and baroclinicity, the flow can be blocked by a range like the northern Appalachians if the undisturbed incident wind speed is around 10 m s^{-1}. Cold advection weakens the barrier effect.

The long-term behavior of the front in strongly blocked cases is described and compared to observations. Because of the background rotation and large-scale temperature advection, blocked solutions cannot become steady in the assumed environment. However, the interface between blocked and unblocked fluid can settle into a balanced configuration in some cases. A simple argument suggests that, in the absence of dissipation, the frontal slope should be similar to that of the ambient ''absolute momentum'' surfaces.

1. Introduction

The purpose of this study is to determine whether coastal mountain ranges could play a crucial role in the type of shallow frontogenesis that is observed during early winter along some seaboards. The best known example, the New England coastal front, was documented by Bosart et al. (1972). Similar mesoscale features have been identified farther south in the Carolinas (Lapenta and Seaman 1990) and Texas (Bosart 1984), along the coast of Norway (Okland 1990), and along the southeast coast of China (Huang 1993). Numerical simulations presented by Garner (1986, hereafter G86) indicate that the topography in most of these regions can fully block a layer of surface air in certain types of idealized on-shore flow. Shallow fronts can then develop upstream as a consequence of the blocking. We wish to extend the investigation begun in G86 to a broader range of

environments. A companion paper (Garner 1999) investigates the specific baroclinic blocking mechanism proposed in that earlier study.

Past research on the relationship between orography and baroclinic airmasses has concentrated on situations where a strong front is already present (e.g., Gross 1994; Egger and Hatt 1994; Haderlein 1989; Zehnder and Bannon 1988; Schumann 1987). Less consideration has been given to the generation of frontal gradients by a mountain circulation when the baroclinic zone is initially much broader than the mountain. G86 concluded that 1) large-scale baroclinicity corresponding to deep warm advection enhances the barrier effect of a topographic ridge and 2) blocking can lead to strong frontogenesis in an atmosphere with initially uniform horizontal stratification. Although the Appalachian ridge averages less than 1000 m above sea level in New England, its extreme length-to-width ratio and the strong inland static stability in early winter enhance the prospects for blocking in that region.

Reproduced in Fig. 1 is a composite sea level pressure analysis compiled by McCarthy (1977) from a number

Corresponding author address: Dr. Stephen T. Garner, NOAA/ GFDL, Princeton University, P.O. Box 308, Princeton, NJ 08542. E-mail: stg@gfdl.gov
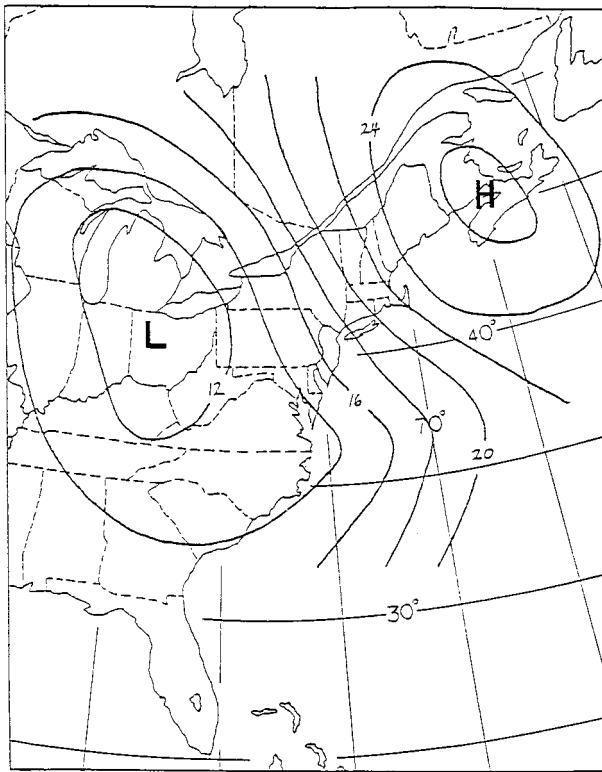
FIG. 1. Composite analysis of sea level pressure during onset of coastal frontogenesis in New England. From McCarthy (1977).

FIG. 2. Schematic depiction of blocking by orography during warm advection. From Bjerknes and Solberg (1921).

of New England cases during the onset of coastal frontogenesis. It was established earlier by Bosart et al. (1972) that the frontogenesis occurs during periods of deep, synoptic-scale warm advection and local pressure falls. The cold-air "damming" that often precedes these periods takes place during cold advection, with pressure rises and relatively weak onshore geostrophic flow (e.g., Bell and Bosart 1989; Doyle and Warner 1993). Bell and Bosart (1989) uncovered a correlation between coastal front in New England and the amplitude of a certain long-wave pattern in the Northern Hemisphere. Bosart (1975) demonstrated that the fronts form through ageostrophic deformation of the temperature. Nielsen and Neilley (1990) used aircraft observations to demonstrate the coastal front's similarity to a density current, particularly in its extreme horizontal wind and temperature gradients and weak thermal wind balance.

Some of the most plausible explanations for the ageostrophic frontogenesis involve the coastal contrast in surface fluxes of momentum (Bosart et al. 1972) and heat (Ballentine 1980; Huang and Raman 1992; Doyle and Warner 1993). Nielsen (1989) analyzed a new set of cases in New England and concluded that, under certain synoptic conditions, these fluxes are crucial in initiating the nongeostrophic deformation and coastal frontogenesis. However, referring to the quantitative criteria developed in G86, he determined that the oro-
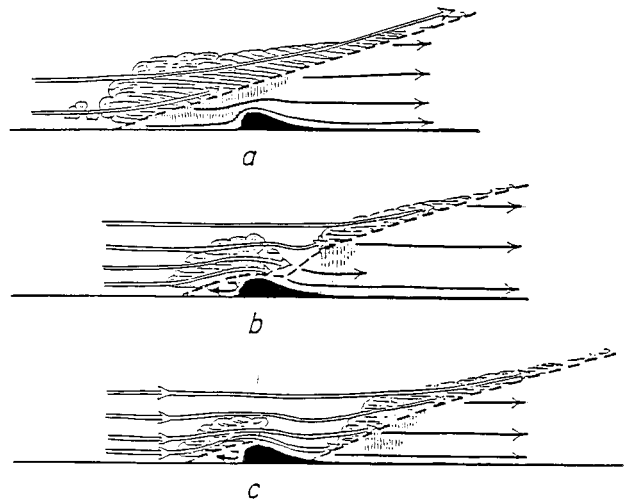
graphic mechanism may be dominant in the relatively warm and windy cases—his "type C" events.

In contrast to the circumstances of coastal frontogenesis, published studies of baroclinic zones modified by orography have dealt almost exclusively with cold advection and cold fronts. The most relevant theoretical study dealing with warm advection may be that of Bjerknes and Solberg (1921). Figure 2 is reproduced from their study. The illustration shows an interface between homogeneous layers of fluid approaching a ridge in the terrain. According to the authors, part of the cold air can become trapped on the windward side of the barrier when the interface advances as a warm front. This picture, though it does not describe frontogenesis, is the simplest idealization of orographic blocking in a baroclinic atmosphere.

Recent studies have provided some limited theoretical support for Bjerknes and Solberg's scenario. In a review paper, Blumen (1992) discusses the canonical problem of a sloping density interface encountering a ridge. His discussion focuses on the circulation at the "nose" of the denser fluid (analogous to a surface cold front) as it reaches the mountain. Earlier, Davies (1984) pointed out that a separate interaction is possible in the same sort of model at some distance from the surface front. He found that the fluid interface may become "grounded" after the denser fluid has fully immersed the barrier. In the Bjerknes–Solberg picture (Fig. 2), the ridge is *initially* immersed and the interface moves in the opposite sense, as a warm front. In that case, depending on the depth of the cold air, grounding may be the first interaction between the front and the ridge.

In layer models, blocking or grounding occurs when an interface or free surface cannot deform rapidly enough, subject to mass and momentum conservation, to clear the obstacle. The flexibility of the interface is determined by a Froude number, which combines the

speed and depth of the fluid layer with the strength of the density jump. Long (1972) and Baines and Davies (1980) find that the blocking effectiveness of a topographic barrier increases sharply as its height approaches that of the undisturbed free surface. The latter authors explain this result in terms of the conversion of kinetic to potential energy during the lifting of the interface. Davies's (1984) solution is for nearly balanced flow and indicates that grounding is most likely if the density contrast is large. In addition to making the interface less flexible, a large density jump decreases its undisturbed slope by increasing the deformation radius. The results of Davies (1984) and Schumann (1987) together show that for both narrow and broad obstacles, steep fluid interfaces are difficult to impede by topographic barriers. The implication is that horizontal stratification (baroclinicity) is ineffective for barrier enhancement if vertical stratification (gravitational stability) is too weak.

Studies have recently begun to consider continuously stratified flows interacting with terrain. Blumen and Gross (1987) describe the distortion of a frontal zone by the steady, balanced circulation forced by a topographic ridge. Since the front is treated as a passive tracer, frontolysis and frontogenesis are predictable from the details of the steady mountain disturbance. Williams et al. (1992) use a primitive-equation model to compare passive-scalar frontal behavior to fully interactive behavior. They find only minimal differences except in the downstream wave train. However, the height of their mountain, like that used in Blumen and Gross (1987), is well below the threshold for upstream stagnation. Nearer the stagnation threshold, the results of G86 indicate significant interaction between the frontal disturbance and the mountain disturbance.

Because coastal fronts usually become steady for a period of time, the steady-state analysis by Xu (1990), originally meant to describe the result of damming during cold advection, also applies to warm-advection upstream frontogenesis. Xu's two-fluid model determines the steady shape of the frontal surface as a function of the vertical diffusivity, surface roughness, and density contrast. It was suggested in G86 that an inviscid blocking front, while never steady in all respects, could nevertheless reach a steady shape. The experiments in G86 were inconclusive about this possibility, but the longer-term experiments to be described here will help to resolve the issue.

The present study uses a multilevel gridpoint model to solve the initial-value problem for a continuously stratified, baroclinic atmosphere. The relationship of the orography to the environment is essentially as in Fig. 2. However, in order to isolate the role of orography, the present strategy is to dispense with any preexisting fronts, coastal contrasts, or geostrophic frontogenetical forcing. This means assuming an environment with uniform stratification in the vertical and horizontal (an infinitely broad baroclinic region), uniform surface eddy flux coefficients, and uniform geostrophic wind. According to Nielsen (1989), type-C coastal fronts differ from the other kinds in that they develop in the absence of a preexisting, synoptic-scale, warm frontal zone. The assumptions of two-dimensional symmetry and an undisturbed synoptic environment tend to exclude such large massifs as the Rocky Mountains and Himalayas. While these can easily "dam" or deflect the surface flow, they are not known for upstream frontogenesis during warm advection.

The present level of idealization is a departure from previous numerical studies of coastal frontogenesis (e.g., Ballentine 1980; Huang and Raman 1992; Huang 1993). The advantage is that it allows a quantitative assessment of one or two simple dynamical mechanisms. In addition to the above assumptions, we will take the Coriolis parameter to be constant. In the hydrostatic, incompressible limit, the response to the topography is then entirely determined by a Froude number (Fr), a Rossby number (Ro), and a nondimensional parameter measuring the baroclinicity. We define the first two as

$$\mathrm{Fr} = Nh_0/u_0 \quad \text{and} \tag{1}$$

$$\mathrm{Ro} = u_0/(fl_0), \tag{2}$$

where h_0 and l_0 are the height and width of the mountain ridge, respectively; f is the Coriolis parameter; N is the undisturbed buoyancy frequency; and u_0 is the undisturbed wind speed in the direction normal to the ridge, which we take to be the x direction. In the barotropic case, the amplitude is fully determined by Fr when Ro is large and by RoFr when Ro is small (Pierrehumbert 1985). Thus, atmospheres with strong static stability (large N) are always easier to block.

The third parameter will be defined as

$$\beta = \Lambda/N, \tag{3}$$

where Λ is the vertical shear of the basic flow parallel to the ridge: $\overline{v}(z) = \Lambda z$. The basic-state Richardson number is thus $\mathrm{Ri} = 1/\beta^2$. The basic potential temperature varies linearly in x in accordance with thermal wind balance. In section 4, we will briefly consider the effect of an additional long-ridge component of temperature gradient.

Pierrehumbert and Wyman (1985) investigated the barotropic version of the initial-value problem. They showed that background rotation by itself tends to inhibit blocking, especially permanent blocking. However, G86 found that baroclinicity can easily overcome this inhibition. Part of the reason is a fairly obvious nonlinear effect: horizontal stratification can be tilted in the vertical cross section to increase the vertical stratification and static stability. Schumann (1987) showed that when a sloping frontal zone is embedded in a continuous background vertical stratification, the barrier effects due to the two features are essentially additive. The increase in vertical stratification is expected to occur on the up-

stream side of the mountain in the case of warm advection. In section 4, we assess a less obvious mechanism for the enhanced barrier effect involving the nonlinearity in the momentum equation.

Specifying a realistic parameter regime can begin with a choice for the nondimensional slope of the topography, RoFr = $Nh_0/(fl_0)$. Separate values of Ro and Fr would then be determined by the choice of u_0, which is more variable than the nondimensional mountain slope. The northern Appalachians are characterized by two ridges, each with a halfwidth of about 40 km. In southern New England, the terrain rises by about 150 and 300 m toward the two summits. If we take f to be 10^{-4} s^{-1} and N to be 2×10^{-2} s^{-1}, we find that RoFr = 3.0 for the western ridge and RoFr = 1.5 for the eastern one. The value of l_0 would be doubled if the valley were eliminated. This may happen, in effect, when the valley is filled with stable, cold air. Using l_0 = 80 km yields RoFr = 1.5. In northern New England, the eastern ridge averages over 800 m, with about the same halfwidth as in the south. In that case, RoFr = 4.0.

In the next section, we first present results from a large set of initial-value experiments with different terrain dimensions and different amounts of baroclinicity. The goal is to determine the minimal conditions for upstream flow stagnation, thereby verifying and extending the results in G86. This is followed by a closer look at solutions with RoFr = 3.0. In section 3, we consider the effects of frictional surface drag and a shallow temperature gradient along the mountain. Section 4 is a discussion about the horizontal scale of the blocked air with and without friction, and section 5 concludes by assessing the realism of the unsteady frontal structures that the model produces in strongly blocked cases.

2. Numerical experiments

In a nonrotating atmosphere with no dissipation, upstream disturbances are either infinite in horizontal scale or unsteady. The term ''upstream influence'' conventionally implies steady changes that are unattenuated in the upstream direction (Long 1955; McIntyre 1972). In a series of numerical experiments, Pierrehumbert and Wyman (1985, hereafter PW) determined that upstream influence is established by horizontally propagating disturbances dominated by long horizontal scales, or ''columnar modes.'' In further initial-value experiments, Garner (1995, hereafter G95) implicated the ''initial surge,'' which is dominated by horizontal momentum and energy fluxes. Unlike the vertical fluxes that establish the near-mountain disturbance and stationary wave train, the upstream fluxes and long horizontal scales are not described by linear theory, that is, the small-Fr limit when Fr is defined by (1). According to G95, the condition for temporary upstream stagnation is Fr > 1.35, while permanent blocking first occurs at about twice

that value. Similar thresholds are reported by PW and Chen et al. (1994).

In a corroboration of Long's hypothesis, PW could find no upstream influence or permanent blocking in simulations *with* background rotation, because the low-frequency part of the disturbance is always confined to a deformation radius upstream. However, G86 found that the addition of ambient baroclinicity slows down the high-frequency transience and, in some cases, allows flows to become permanently blocked. These cases are fundamentally different from nonrotating blocked flows. Not only is the scale of the upstream disturbance finite, but there is constant acceleration over time of the ''drainage'' flow along the ridge, as well as unlimited deformation of the temperature field even if the cross-mountain velocity becomes locally steady. It was suggested in G86 that a blocked region could reach a finite limiting radius. We will reconsider this possibility in section 4 in the light of the more recent theoretical work by Xu (1990).

The numerical model used in the G86 study is not practical for an extensive search of parameter space because it was designed with a computationally inefficient Lagrangian grid in order to resolve frontal gradients. The present model is described briefly in the next subsection. It adds a basic density gradient, f-plane effects, and stretched vertical resolution to the gridpoint model used in G95.

a. Model description

The model is based on anelastic vorticity-streamfunction equations (e.g., Kim et al. 1993) with a terrain-following vertical coordinate. The potential buoyancy, $b \equiv g\theta/\theta_0$ (with θ the potential temperature and g the acceleration of gravity), and meridional wind component, v, are defined at doubly staggered points relative to the horizontal vorticity, ω, and mass streamfunction ψ. The time-stepping is leapfrog, with a trapezoidal correction of b and v (Kurihara 1965). The grid is stretched in the vertical to provide 2 times finer resolution near the ground than at the upper boundary. The average grid spacing is similar to that in the studies by PW and G95, namely $\Delta x = 0.2l_0$ and $\Delta z = 0.2h_g$, where $h_g \equiv u_0/N$.

For computational purposes, scale-sensitive diffusion is applied to the velocity variables, v and ω, with the ratio of horizontal to vertical diffusivity set at 100. For example,

$$d\omega/dt = fv_z - b_x - w\omega/h_d + K_0(100\omega_{xx} + \omega_{zz}), \quad (4)$$

where K_0 is the background diffusivity and h_d is the density scale height. The diffusivity is increased locally for all three prognostic variables (including b) when the vertical stratification falls below 10% of the undisturbed value. The details of this scheme, a crude convective adjustment, are not very important for systematic upstream effects. In G95, K_0 was chosen so that the Reynolds number based on the mountain height,

$$\mathrm{Re} \equiv h_0^2 u_0 / (l_o K_0), \tag{5}$$

was the same for all experiments, namely $\mathrm{Re} = 50$. For the purpose of finding stagnation thresholds in the next subsection, we prefer to fix $\mathrm{Re}_g \equiv h_g^2 u_0 / (l_o K_0)$, where $h_g \equiv u_0/N$, in order that the viscosity has a similar effect on the internal waves for all Fr. The present results are for $\mathrm{Re}_g = 100$, equivalent to $\mathrm{Re} = 100\mathrm{Fr}^2$.

In limited-area modeling, solutions must be free of any significant effects from the artificial boundaries. Open lateral boundaries are approximated here using a method suggested by Orlanski (1976) and refined by Raymond and Kuo (1984) while the upper boundary condition is a generalization of the Klemp–Durran (1983) scheme that takes into account the background rotation and large-scale baroclinicity (Garner 1986b). The lateral boundaries are placed at $x = \pm 20l_0$ and the upper boundary at $z = 15h_g$. A few experiments were conducted with larger domains and with sponge regions at the upper and lateral boundaries in order to check on the effectiveness of the radiation conditions.

Initial conditions are specified by $\overline{b}(x, z) = N^2[z + (f/N)\beta x]$ and $\overline{v}(z) = \beta Nz$, where β is defined by (3). We are only interested in $|\beta| < 1$, which is necessary for stability to slant-convective overturning (e.g., Bennetts and Hoskins 1979). Since there is no dynamical distinction between westerly and easterly flow on an f plane, it is assumed that $u = u_0 > 0$ for the basic wind. The case of warm advection then has $\beta < 0$. For the canonical problem of finding parameter thresholds for surface stagnation, we use an infinite density scale height. Later, in examining frontogenesis in blocked flows, the more realistic value, $h_d = 16h_0$, is used.

The terrain is specified by a Gaussian profile, $h(x) = h_0 \exp(-x^2/l_0^2)$. The mountain width determines an "advective" time unit,

$$\tau_a = l_0/u_0, \tag{6}$$

which is useful for measuring transient phenomena. For $l_0 = 40$ km, this comes to about 1.8 h when $u_0 = 10$ m s^{-1}. The basic wind in x will be started impulsively. Finally, we let $u_0/(Nl_0) = \mathrm{Fr}^{-1}(h_0/l_0) = 0.05$, to complete the specification of parameters. This ensures nearly hydrostatic conditions everywhere except possibly in the wave breaking regions.

b. Stagnation and blocking

It is fundamental to determine the minimum Fr for upstream stagnation as a function of both Ro and β. Comparing stagnation thresholds for different Ro or β reveals the extent to which background rotation and baroclinicity weaken or strengthen the initial upstream surge. As mentioned above, this is the event that establishes the time-mean conditions upstream and is crucial for blocking in the nonrotating case (G95).

The results of numerous initial-value experiments are summarized in Fig. 3. The abscissa is Ro^{-1}, so the in-
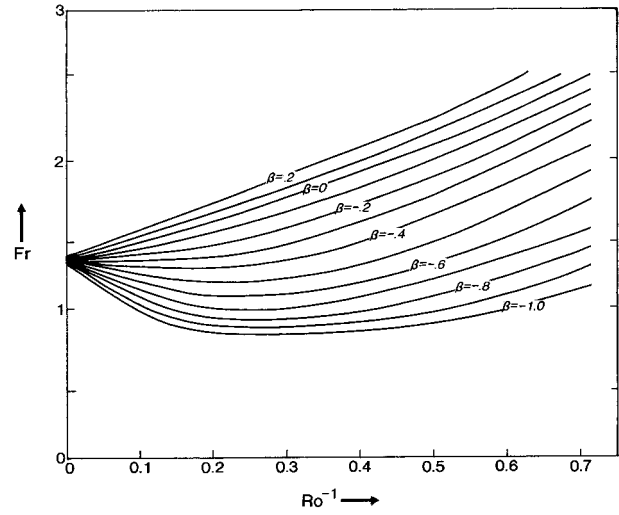

FIG. 3. Regime boundaries, labeled by the baroclinicity β, between solutions with and without upstream stagnation as a function of Ro^{-1} $\equiv fl_0/u_0$ and Fr $\equiv Nh_0/u_0$. Surface flow stagnation occurs in the region above each boundary.

fluence of rotation increases to the right. The ordinate is the nondimensional mountain height, Fr, so the influence of the stable stratification increases upward. The contours are drawn between all cases with stagnation events for the given baroclinicity, β, and all cases without stagnation. It can be seen that, for a given Ro^{-1}, the stagnation threshold, say Fr$_s$, decreases monotonically as β becomes more negative, that is, as the warm advection becomes stronger. No results have been plotted for $\beta > 0.2$ because the threshold becomes highly insensitive to baroclinicity in cold advection. The curve for $\beta = 0$ is reasonably consistent with the barotropic results in PW's Fig. 14.

In the nonrotating limit (Ro$^{-1} = 0$), the model reproduces Fr$_s = 1.35$ from G95's Fig. 4a. Holding Fr constant, we see that rotation generally inhibits upstream stagnation, and that this sensitivity increases somewhat with increasing Ro^{-1}. However, there is a significant dip in the curves for large $|\beta|$, indicating an enhancement of the barrier effect up to a certain rate of rotation if there is sufficient warm advection. This is an *indirect* effect of background rotation. At Ro$^{-1} = 0$, the vertical shear, $d\overline{v}/dz$, is not associated with a temperature gradient and the cross-mountain wind is, therefore, not fully coupled to v'. As rotation is introduced, the blocking due to baroclinicity becomes significant more rapidly than the countervailing inertial restoring force discussed previously.

Points with the same nondimensional mountain slope Ro $\times$ Fr lie on straight lines through the origin in Fig. 3. At Ro$^{-1} = 0.5$, the critical slope Ro $\times$ Fr$_s$, ranges between 1.8 and 4.2 as β increases from -1 to 0. Most of the estimates of Ro $\times$ Fr mentioned in the introduction fall within this range. Hence, upstream stagnation due to "realistic" coastal mountains is possible even in
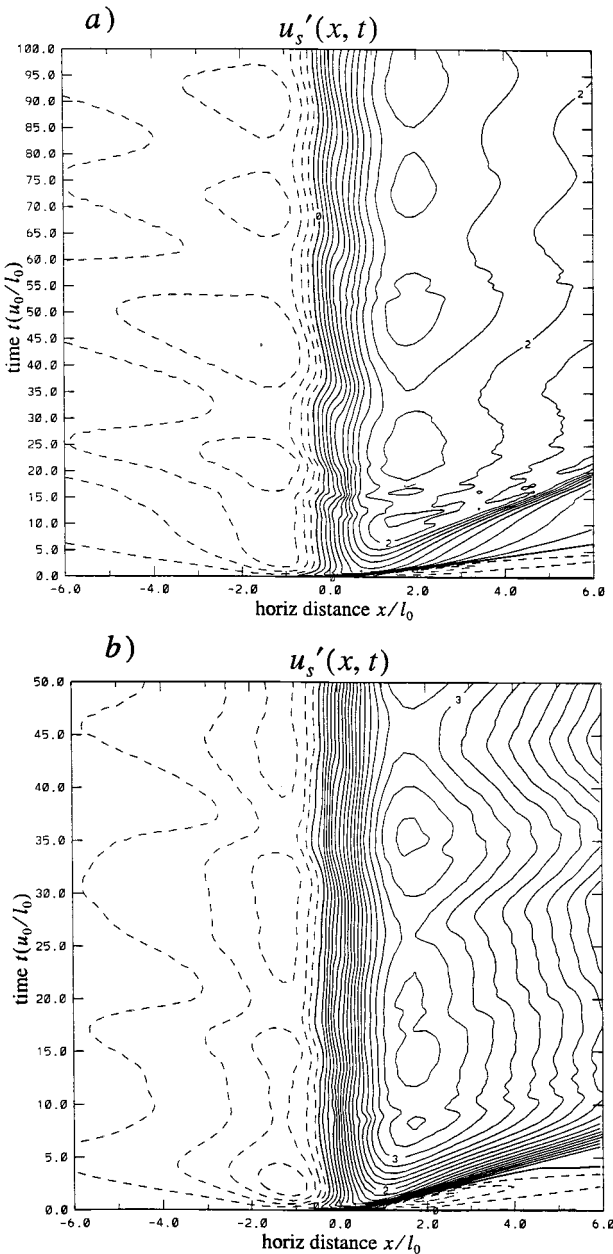
FIG. 4. Perturbation horizontal surface velocity u'_s as a function of time and distance from the mountain center for the case (a) Ro = ∞, Fr = 1.3 and (b) Ro = 2.0, Fr = 2.0. The horizontal axis is scaled by the mountain halfwidth, l_0, and the vertical axis by the advective time unit, $\tau_a \equiv l_0/u_0$. Contour interval: $\delta u = 0.2u_0$.

cases where the background rotation is significant. For the cases with weak baroclinicity, the blocking is either temporary or delayed past any realistic development time. Hence, permanent blocking in a reasonable time by realistic mountains requires strong baroclinicity.

c. Barotropic experiments

The separate effect of the background rotation, as distinguished from the baroclinicity, can be seen in Fig. 4.

Shown are time–distance plots of the surface wind perturbation, $u'_s(x, t)$, in barotropic experiments with Ro = ∞ (Fig. 4a) and Ro = 2 (Fig. 4b). The mountain is centered at $x = 0$. The number Fr is chosen just below the upstream stagnation threshold in each case. Notice the persistent low-frequency variability in both solutions. It was shown in G95 that in the nonrotating solution, this low-frequency signal is related to the wave breaking near the mountain, but it was not clear what determined its timescale. In the rotating solution, the upstream transience has roughly the inertial timescale of $2\pi\text{Ro}\tau_a$ [about 12.5 time units, as defined by (5)]. A very similar plot for Fr = 2.5, which is somewhat beyond the stagnation threshold, appears in Fig. 11 of Pierrehumbert and Wyman (1985). The persistence of the oscillation at the same location suggests continuing excitation, probably by the wave breaking just downstream. Experiments show that the inertial frequency dominates the upstream transience all the way up to Ro ≈ 5.

The downstream perturbation has a maximum near $x = 2l_0$ in both barotropic solutions. In the rotating case, the time-mean downstream pattern is a nonlinear inertial lee wave, with u'_s changing sign approximately Roπ units downstream of the maximum (just beyond the edge of the plot). If Fr exceeds the "high drag" threshold of approximately 0.75, increasing Ro toward the nonrotating limit eventually causes this first convergence zone to take on characteristics of an internal hydraulic jump, including active turbulence and a sharp drop in perturbation energy across the zone (e.g., Durran 1986, G95). The case Ro = 2 in Fig. 4 is close enough to the nonrotating limit to have these characteristics. The final location of the internal jump was found to depend on both the rate of rotation (Ro) and the explicit viscosity (Re). In the limit Ro → 0, the steady cross-mountain flow perturbation and stationary lee waves disappear. As the lee waves and wave breaking disappear, so does the associated upstream transience. Hence, persistent upstream transience is a significant part of the disturbance only at large Ro.

The experiments summarized in Fig. 4 were carried out to an elapsed time of $t = 40\tau_a$. In some cases, the choice of cutoff time may have affected the results. In cases of strong warm advection, the first surface stagnation event may not occur during the first or even second cycle in the upstream transience and may, therefore, be overlooked in a limited-time experiment. However, since the minimum surface velocity does not vary greatly between the cycles of transience, the effect on the thresholds is believed to be small. The model may not be reliable at this degree of detail.

d. Baroclinic experiments

The time–distance plots of u'_s in Fig. 5 are from three simulations with the same (Ro, Fr) = (2, 1.5) but different values of β. The background viscosity is such that Re$_g$ = 50 and we have used a finite density scale
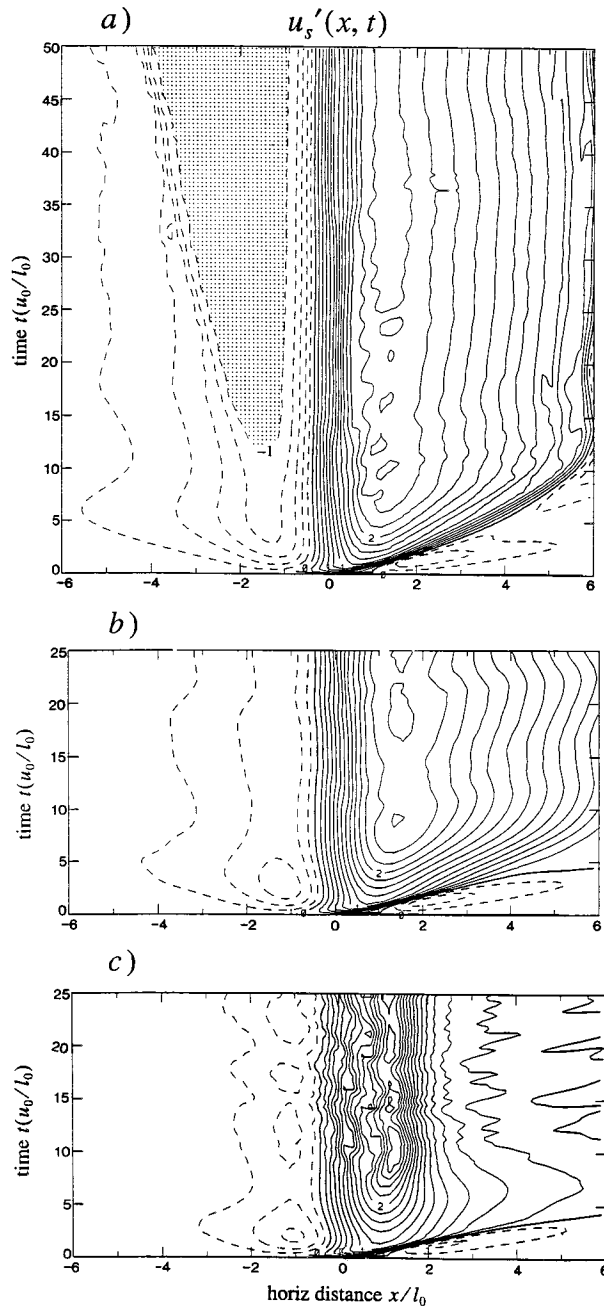
FIG. 5. Perturbation horizontal surface velocity u'_s as a function of time and distance from the mountain center for the case (Ro, Fr) = (2.0, 1.5) with (a) $\beta = -0.6$, (b) $\beta = 0$, and (c) $\beta = 0.6$. Stippling indicates a region of stagnated or reversed flow. Axes and contour interval as in Fig. 4.

height, $h_d = 16h_0$. For these parameters, temporary blocking first occurs near $\beta = -0.5$, similar to the result indicated in Fig. 3 for $\mathrm{Re}_g = 100$ and constant background density. The case $\beta = -0.6$ (Fig. 5a) is permanently blocked after $t = 12\tau_a$, whereas the other two solutions, $\beta = 0$ and $\beta = 0.6$, maintain a positive cross-mountain wind, $u_s > 0.3u_0$. In the nonrotating limit and

in barotropic cases, the threshold for temporary blocking is farther from the threshold for permanent blocking (PW, G95). The baroclinicity in the warm-advection case strongly suppresses the upstream inertial oscillation and systematically amplifies the disturbance there. A brief period of temporary stagnation at around $t = 4\tau_a$ is the only vestige of oscillatory behavior. The flow over the mountain remains nearly laminar. In the barotropic case, inertial transience is prominent, while in the cold-advection solution, it is obscured by the higher-frequency wave breaking transience. Note that the leeside hydraulic jump (tight gradient of u'_s detached from the primary wave train) is missing in the case of cold advection (Fig. 5c). An internal jump in this situation would involve the lifting of relatively cold surface air and may not be possible.

The total buoyancy and the perturbation long-ridge velocity at the surface in the warm-advection experiment are plotted as a function of time and distance in Fig. 6. There is frontogenesis at the upstream edge of the blocked region (Fig. 6a), presumably limited by the grid resolution. Warm air is continuously introduced into the blocked region near the mountain summit and also at the front. However, with no explicit thermal diffusivity, the model manages to maintain a nearly constant *minimum* temperature in this air. The continuing expansion of the blocked region is not typical of coastal fronts (Nielsen and Neilley 1990). This unrealistic aspect of the solution is found to be sensitive to diffusivity. With smaller diffusivity or with spatially varying surface frictional drag, the size of the blocked region can be stabilized earlier. In section 4, we will consider how the limiting scale of a stabilized blocked region might be determined.

Horizontal momentum diffusion weakens the frontogenesis in the v field (Fig. 6b). Without any diffusion or surface drag, the long-ridge surface wind should vary according to

$$\partial v'_s/\partial t = -\mathrm{Ro}^{-1}u'_s, \tag{7}$$

in which time is scaled by τ_a and velocity by u_0, as in the figure. In the present solution we have $\mathrm{Ro}^{-1} = 0.5$ and, in the blocked region, $u'_s \approx -1$, so that (7) is satisfied at early times. Later, however, the acceleration is reduced by the diffusion in an increasingly shallow blocked layer. This result could be qualitatively realistic except for the effect of the free-slip lower-boundary condition on velocity. Free slip puts the maximum long-ridge flow on the ground and allows it to become unrealistically strong. A more realistic solution with explicit frictional surface drag will be presented in section 4. The absence of an upstream inertial oscillation associated with v' is due not only to the frictional dissipation, but also, as we will see below, to the developing pressure perturbation.
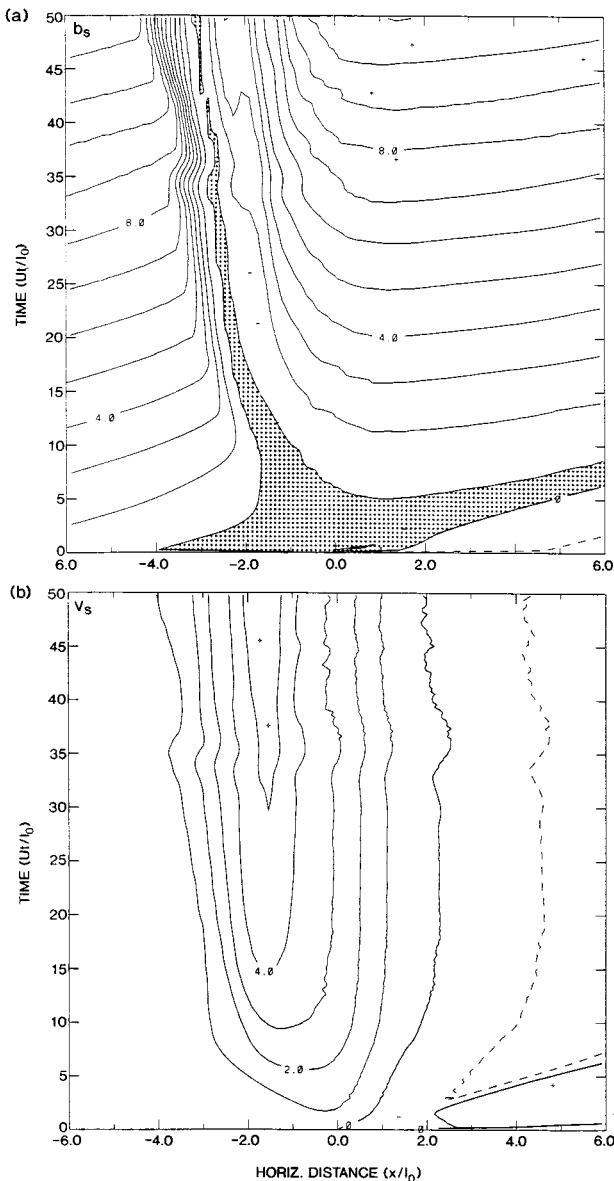
FIG. 6. Time–distance plots of (a) surface buoyancy, b_s, and (b) long-ridge surface velocity, v_s, in the case (Ro, Fr) = (2.0, 1.5) of Fig. 5 but with large-scale warm advection, $\beta = -0.7$. Values of b_s between 0 and 1.0 are stippled. Contour intervals: $\delta v = 1.0u_0$ and $\delta b = 1.0N^2h_0$.

e. Vertical structure

Vertical cross sections of a blocked solution with (Ro, Fr) = (2, 1.5) and $\beta = -0.7$ are shown in Fig. 7. The axes are scaled by l_0 and h_0. For this solution and those in section 4, we have used a finite density scale height, $h_d = 16h_0$. The blocked air ($u_s' \leq -1.0u_0$) extends in a shallow layer to $x \approx -3.0l_0$. Much of this air originated on the mountain and failed to cross it during the start-up. The frontal zone in Fig. 7b is entirely the result of ageostrophic deformation; since u' is all ageostrophic, there is no geostrophic deformation in the

model. A low-level convergence feature resembling the internal hydraulic jump familiar in the barotropic solutions is just out of the picture to the right in Fig. 7a.

Horizontal trajectories veer to the left near the front, as implied by the positive values of v' in Fig. 7c. As seen before in the case of $\beta = -0.6$ (Fig. 6b), this wind is several times stronger than the ambient flow across the mountain, with a maximum of $4.4u_0$ at the time shown. The horizontal pressure gradient for the blocked solution is shown in Fig. 7d. The maximum value of the geostrophic wind $v_g' = (f\rho_0)^{-1}p_x'$ associated with the surface pressure gradient is $v_g' = 4.0u_0$ near $x = -2.2l$. Hence, some of the long-ridge motion in the blocked region is geostrophically adjusted.

f. Topographic drag

The blocked solution, with its wave breaking, downstream "shooting flow," and hydraulic jump, fits the qualitative description of high-drag flow over isolated terrain (e.g., Durran 1986; Smith 1985). Drag depends on the correlation between the pressure perturbation and terrain slope, as well as the amplitude of these quantities. In barotropic conditions, the drag due to an isolated mountain is known to have a high sensitivity to Froude number because of a sharp transition in the flow configuration as wave breaking sets in (e.g., Durran 1986, G95). Here we have an opportunity to test the sensitivity of the drag to ambient baroclinicity. The method of diagnosing the pressure and topographic drag is described in G95.

In Fig. 8, the steady-state model drag D, normalized by $Nh_0^2u_0$, is graphed versus β for Ro = 2 and three different values of Fr. The case Fr = 0.02 may be considered linear. The highest mountain shown, Fr = 0.8, is just below the stagnation threshold for the strongest warm advection (cf. Fig. 3). In the linear case, the normalized drag changes only slightly, from 0.8 to approximately 1.0, as baroclinicity is introduced with either sign. However, at finite amplitude, the effect of baroclinicity clearly depends on the sign. Whereas D has little sensitivity to Fr in cold advection, it roughly doubles, to $D \approx 2$, between the linear solution and Fr = 0.8 in warm advection. For the sake of comparison, note that high-drag solutions without background rotation have $D \approx 3$ up to Fr = 3 (G95). In the warm-advection solutions for Fr = 0.8, the downstream shooting flow and extreme low pressure in the lee are also typical of high-drag flows in barotropic environments.

As suggested by the curve for Fr = 0.4, the drag varies smoothly up to Fr = 0.8 for all β. Hence, by this measure, there is no regime transition between the linear and nonlinear cases, even though the wave breaking threshold falls within the Fr interval for most of the warm-advection cases. In nonrotating solutions, the wave breaking threshold is always marked by a sharp transition to high drag, as mentioned above. In rotating solutions, sharp transitions still appear, but only at larger
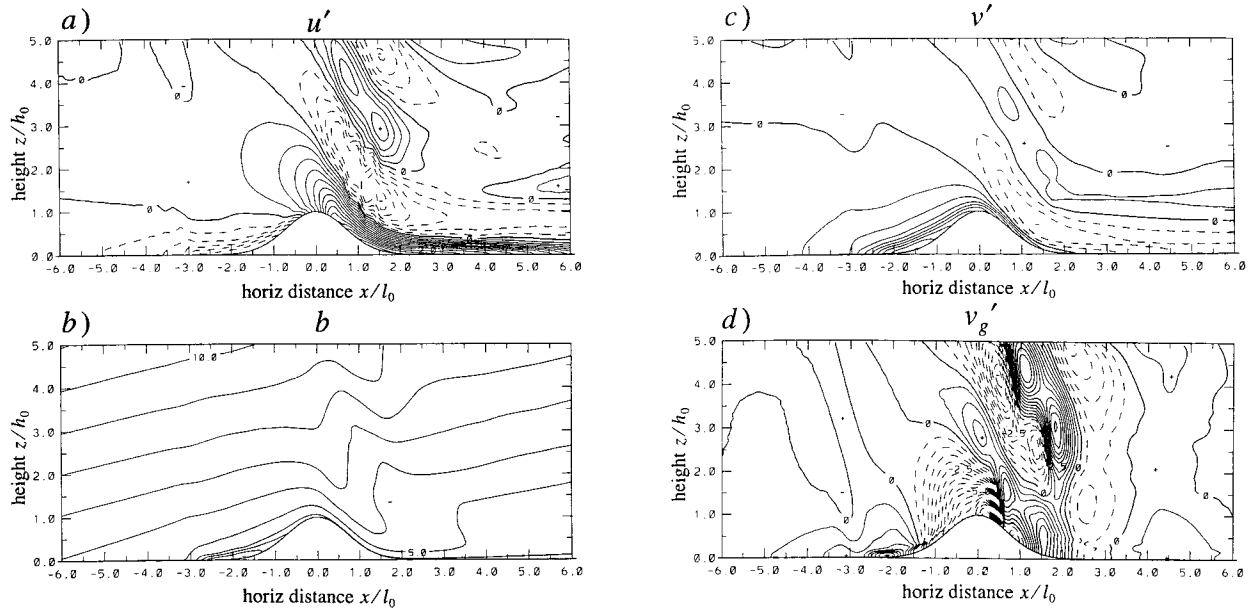
FIG. 7. Vertical cross sections of (a) u', (b) b, (c) v', and (d) v'_g at $t = 20\tau_a$ from the same warm-advection case as in Fig. 6. Contour intervals: $\delta u = 0.2u_0$, $\delta b = 1.0N^2 h_0$, and $\delta v = 0.5u_0$.
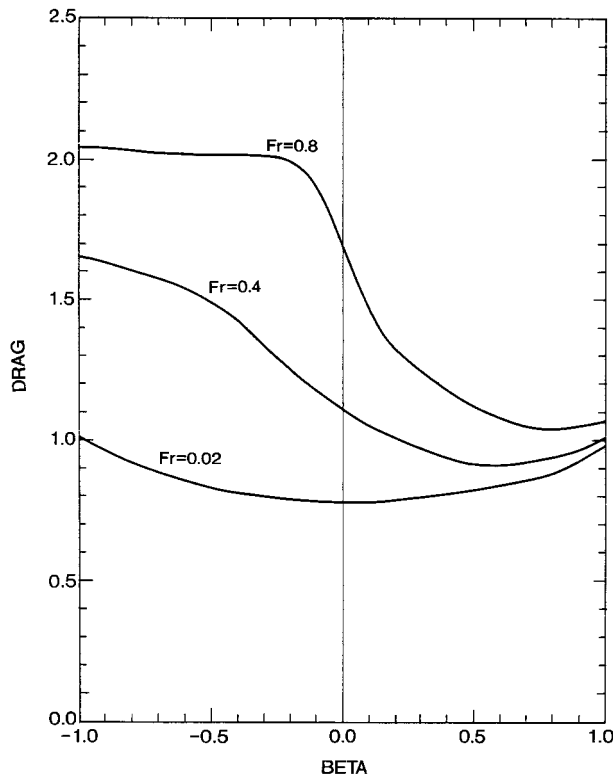

FIG. 8. Total topographic drag as a function of β in steady solutions with Ro = 2.0 and Fr = 0.02, Fr = 0.4, and Fr = 0.8. Drag is normalized by $Nh_0^2 u_0$.

values of Fr and only for cold advection. For example, in steady solutions for $\beta = 0.6$ (not shown) the drag jumps from 1.5 to 3.5 as Fr increases from 1.2 to 1.5 across the breaking threshold (near 1.3). There is no such transition in warm advection.

In a limited-area model, all or part of the drag can be balanced by the Coriolis force due to flow in the direction of the ridge axis, that is, by $\iint fv'\,dx\,dz \equiv f[v']$. Allowing $[v'] \neq 0$ is the same as allowing a transfer of mountain torque beyond the model boundaries through geostrophic adjustment and gravity–inertia wave radiation. Export of momentum deficit by these processes (not entirely distinct) depends on the boundary profiles of u' and the pressure p'. The treatment of the boundaries is thought to be fairly accurate within the broad constraints of the model; however, the two-dimensional symmetry may have an unrealistic effect on the geostrophic adjustment. In a three-dimensional, limited-area model, $[v']$ would be linked to temporal variations of the large-scale, cross-mountain wind, whereas in the present model the geostrophic component, u_0, is not allowed to change. This could affect the steady-state total drag, as well as the details of the momentum flux profiles.

3. Realistic modifications of the environment

For typical values of f and N, the horizontal temperature gradient in the model environment is about $0.04|\beta|$ in units of degrees Celcius per kilometer. The observations in New England show a maximum contrast of about 20°C at low levels, where sea surface heating most strongly affects the large-scale temperature pat-

tern. If the horizontal gradient is uniform, this total contrast corresponds to a distance of $500/|\beta|$ km. Hence if $l_0 = 40$ km, the baroclinic solution is realistic out to a time of no more than $t = (12.5/|\beta|)\tau_a$. In the case $\beta = -0.7$ highlighted in section 2, this time limit comes to $t = 18\tau_a = 18\text{Ro}^{-1}f^{-1}$. The main reason for choosing $\text{Ro}^{-1} = 0.5$ in section 3 was to keep this time close to 1 day, which is roughly the observed spinup time of the coastal front in New England. However, after this much time, the simulated front is still weaker and shallower than observed. In this section we consider two additional environmental features, namely, surface frictional drag and long-ridge temperature gradient. We are interested in whether these provide significant mechanisms for strengthening the blocking and frontogenesis.

Surface drag is introduced by replacing the free-slip condition with

$$K_0 \partial \mathbf{V}_s/\partial z = C_D |\mathbf{V}_s| \mathbf{V}_s, \tag{8}$$

which is the standard bulk aerodynamic parameterization. The dimensionless parameter C_D is chosen large enough to reduce the maximum of v in the blocked air to a realistic value comparable to u_0. By trial and error, this was found to be $C_D \approx 0.01$, although the solutions showed little sensitivity for $0.002 < C_D < 0.02$. To avoid a frictional boundary layer at the upstream model boundary, we keep $C_D = 0$ in $x < -10l_0$. The transition at $x = -10l_0$ is far enough upstream to have little effect on the surface front during the time of the experiment. In order to deepen the frictional boundary layer, the vertical diffusivity is increased by a factor of 4, so that $\text{Re}_g = 12.5$. According to Xu (1990), using a more realistic, height-dependent diffusivity has a minor effect on the shape of the front. Since the velocity in (8) refers to the total wind, the value of $\bar{v}$ at the ground becomes relevant. Here we take $\bar{v} = 0$ at $z = 0$.

The surface friction solution at $t = 20\tau_a$ is plotted in Fig. 9. The cold pool is deeper and extends much farther upstream than in the free-slip experiment (Fig. 7). The coldest temperature in the blocked air is $0.5N^2h_0$. This is about the same as in the free-slip solution, indicating a similar time of initial blocking at the lowest grid points. However, the volume of air with, say, $b < 3.0N^2h_0$ remaining on the windward side is much greater in the present solution. Thus, the reduction of v by frictional drag deepens the blocked flow and enhances the spreading upstream.

Next we consider the impact of a temperature gradient along the ridge. In the Northern Hemisphere, the direction of the long-ridge wind perturbation is such that the blocked region could be made colder by orienting the additional gradient from right to left looking downwind across the ridge. If the mean surface wind is easterly, as in the case of eastern seaboard coastal fronts, this choice puts colder air at higher latitudes, as is typical.

A long-ridge temperature gradient is normally balanced by an x component of vertical shear. However, we will avoid the complication of vertical shear across

the ridge by assuming that thermal wind balance in y is disrupted by a frictional boundary layer. This is reasonable if the temperature gradient is shallow. We define $\gamma \equiv (\partial\bar{b}*/\partial y*)/fN$, which is analogous to β. Thus the undisturbed buoyancy is taken to be

$$\bar{b} = \text{Fr}^{-1}(z + \beta x + \gamma e^{-z/d}y), \tag{9}$$

in units of N^2h_0 for some constant vertical scale d (x and z are scaled by $\mathbf{u}_0/f$ and u_0/N respectively). The exponential height dependence in (9) makes $\partial\bar{b}/\partial z$ a function of y. Therefore, to be consistent with the assumption of a y-independent perturbation, we require that $|\gamma\eta| \ll d$ over a distance $|\eta| \gg 1$.

A solution for $\gamma = 0.2$ and $d = 3$ is shown in Fig. 10. The other parameters are $(\text{Ro}, \text{Fr}) = (2, 1.5)$ and $\beta = -0.7$. At this value of Fr, the vertical e-folding scale of the long-ridge temperature gradient is exactly twice the mountain height. Since the effect of γ depends on the development of a long-ridge velocity perturbation, we retain the surface drag, though at a lower value, $C_D = 0.005$. The solution shows a minimum temperature in the blocked air of 0.4, only slightly colder than in the previous experiment. However, cold advection along the ridge increases the volume of the coldest blocked air (cf. the contour for $b = 1.0$ in Figs. 9b and 10) and slightly intensifies the surface front.

4. Discussion

It was mentioned in the introduction that blocked solutions can never become perfectly steady because of the accelerating long-ridge flow, v, as well as the unceasing deformation of the temperature in and around the blocked air. However, it is still possible in principle for the shape of the interface between blocked and unblocked fluid to equilibrate via thermal wind balance or, perhaps, a more complicated balance involving surface frictional drag. In G86, an assumption of thermal wind balance led to a prediction that the interface should become steady with the same slope as the ambient absolute momentum surfaces. The argument is straightforward. According to Margules's principle, the slope of a frontal discontinuity in geostrophic and hydrostatic balance is

$$\alpha = -\frac{f\Delta M}{\Delta b}, \tag{10}$$

where Δ denotes a (time dependent) jump across the front. By exploiting the Lagrangian invariance of $M - u_0t$ and b and neglecting vertical displacements, we can substitute $\Delta M = \bar{M}_x L_i$ and $\Delta b = \bar{b}_x L_i$, where L_i is the initial horizontal distance between fluid particles that have come together at the front. Thermal wind balance in the basic state implies $\bar{b}_x = f\bar{M}_z$. Hence (10) becomes

$$\alpha = \alpha_{\bar{M}}, \tag{11}$$

where $\alpha_{\bar{M}} \equiv -\bar{M}_x/\bar{M}_z$, the slope of the basic absolute momentum surfaces.

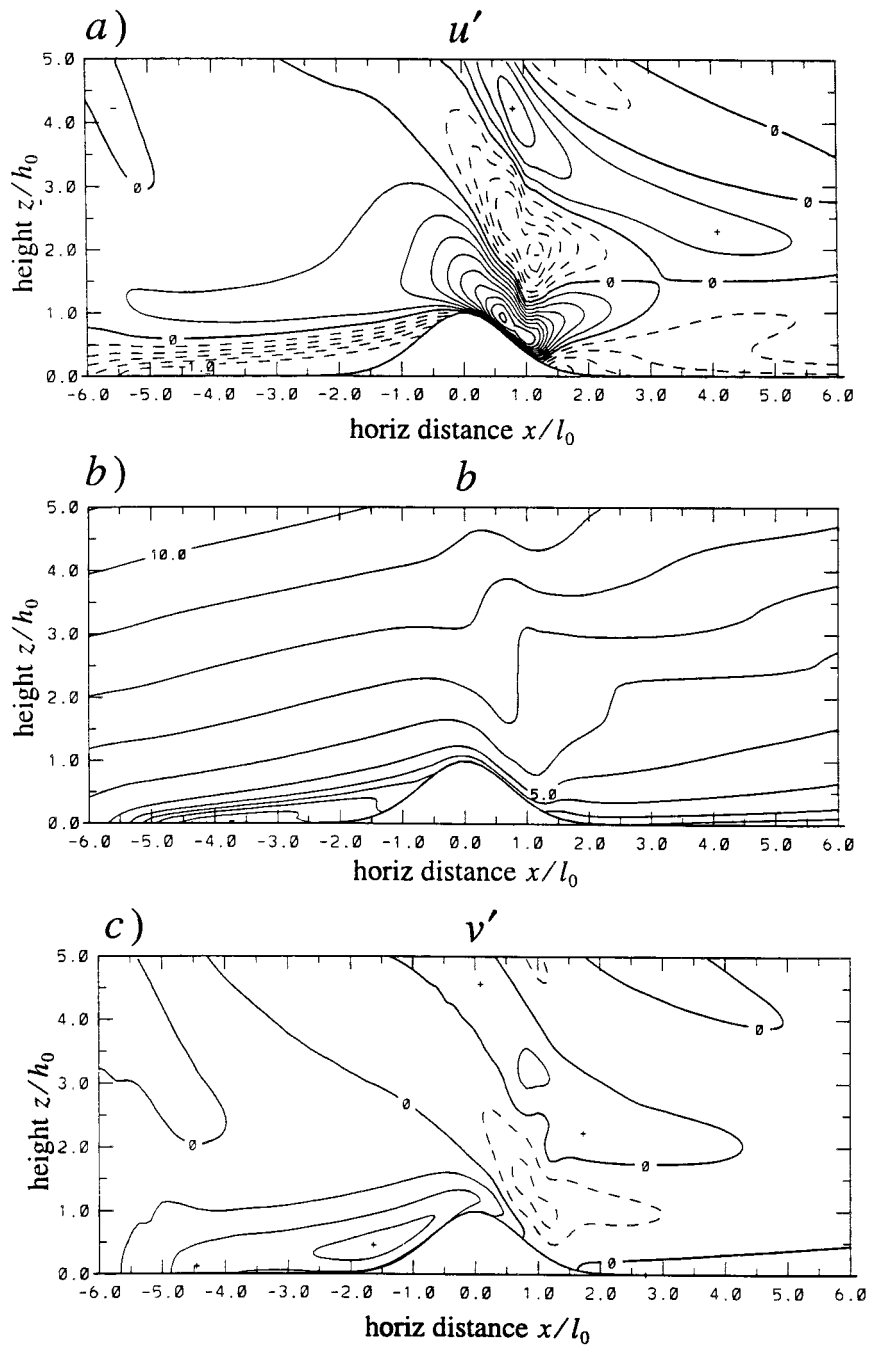The prediction (11) should be poorest in the most

FIG. 9. Vertical cross sections of (a) u', (b) b, and (c) v' for the same case (Ro, Fr) = (2.0, 1.5) and $\beta = -0.7$ of Fig. 7, but with surface frictional drag included using $C_D = 0.01$ everywhere downstream of $x = -10l_0$. Contour intervals: $\delta u = 0.2u_0$ and $\delta b = 1.0N^2 h_0$. Axes as in Fig. 7.

viscous solutions, where (10) is not well satisfied and M and b are not exactly conserved. In the nearly inviscid blocked solution described in section 2c, a large fraction of the long-ridge velocity is in balance with the pressure field ($v \approx v_g$), as seen in Fig. 7. Figure 11 shows the v and v_g fields for the same experiment at $t = 60\tau_a$, when the blocked fluid has stopped spreading. Between

$x = -2.5l_0$ and $x = -3.0l_0$, much of the flow near the ground is approximately balanced, although there is an obvious one-grid-level boundary layer in v_g associated with the free-slip vertical viscosity parameterization.

Note that the frontal region is considerably less steep than the ambient M surfaces, whose slope is indicated by the heavy line. The main problem with (11) is not
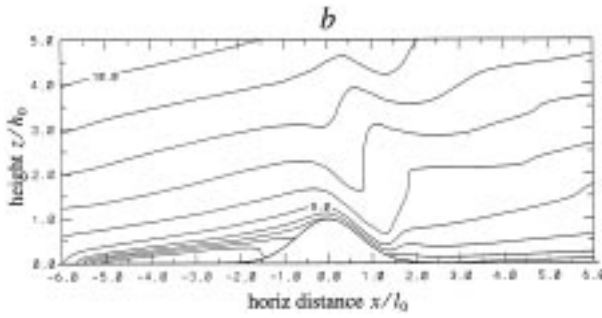
FIG. 10. Vertical cross sections of b from the same warm-advection case as in Fig. 7 but with long-ridge baroclinicity added using $\gamma = 0.2$, and $C_D = 0.005$.

thermal wind imbalance due to viscosity, but nonconservation of M and b. If L_i is reduced to, say, $\varepsilon_v L_i$ and $\varepsilon_b L_i$ in the above estimates for the respective frontal contrasts, then the predicted slope α becomes multiplied by $\varepsilon_v/\varepsilon_b$. In the present solutions with no explicit thermal diffusion, the frontal contrast in v is affected more than the temperature contrast (cf. Fig. 6), so that $\varepsilon_v/\varepsilon_b < 1$ and the steady front should slump relative to the M surfaces.

Several cases with surface frictional drag were run to $t = 80\tau_a$ to see how a more realistic lower boundary changes the long-term behavior. There was no indication of convergence to a steady frontal configuration in these experiments. This is consistent with the analysis by Xu (1990). His two-fluid, f-plane model gives the shape of a steady density interface subject to vertically varying vertical diffusivity of temperature and velocity and a no-slip surface boundary condition. He finds that the interface shape is more sensitive to the density contrast than to any of the details of the friction parameterization. Xu's result implies that the present simulations could never produce steady frontal slopes unless the large-scale temperature gradient vanished during the experiment.

A different way to equilibrate the frontal shape is to move the C_D transition closer to the mountain. In the solution shown in Fig. 12, the transition is located at $x = -4l_0$ and the frontal position has become steady. The interior diffusivity is uniform and relatively strong. Notice the surface-based jet in the v field on the free-slip side of the transition. This may be a qualitatively realistic picture if the transition point is interpreted as a coastline. However, the long time required to reach this state ($t = 40\tau_a$) is still unrealistic.

5. Summary and conclusions

The modeling has shown that even modest terrain at Ro = 2 can produce shallow, ageostrophic frontogenesis upstream within a broad zone of strong warm advection. We have concentrated on mountain ranges with aspect ratio $h_0/l_0 = 3.0(f/N)$, which is fairly representative of the Appalachians if we assume $N = 0.02$ s^{-1}. Although
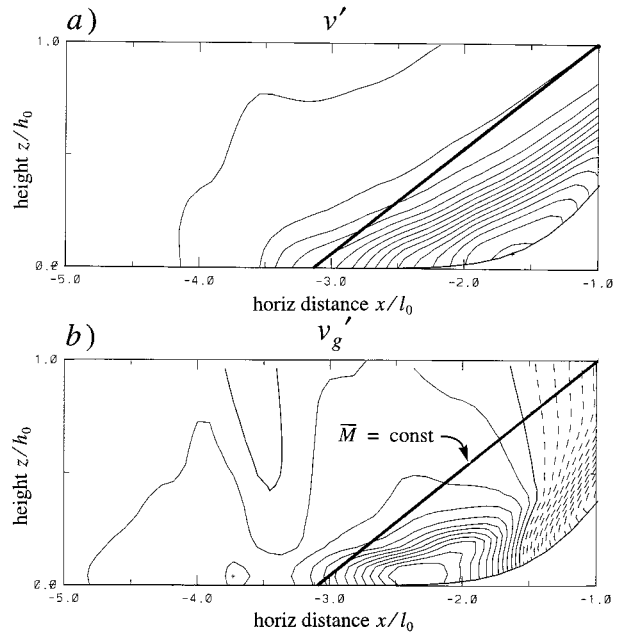

FIG. 11. Vertical profiles (a) v'_g and (b) v' at $t = 60\tau_a$ in same experiment as in Fig. 7 but at a later time, $t = 60\tau_a$. Heavy line indicates slope of ambient absolute momentum surfaces. Contour interval as in Fig. 7.

this is a large value for the lower-tropospheric static stability, it is not unusual over land in the winter. The choice Ro = 2 was motivated by observations of the total temperature contrast and approximate 1-day spinup time of coastal fronts. Since $u_0 = \mathrm{Ro} f l_0$, the choice implies a cross-ridge mean wind of the order of 10 m s^{-1}. This is
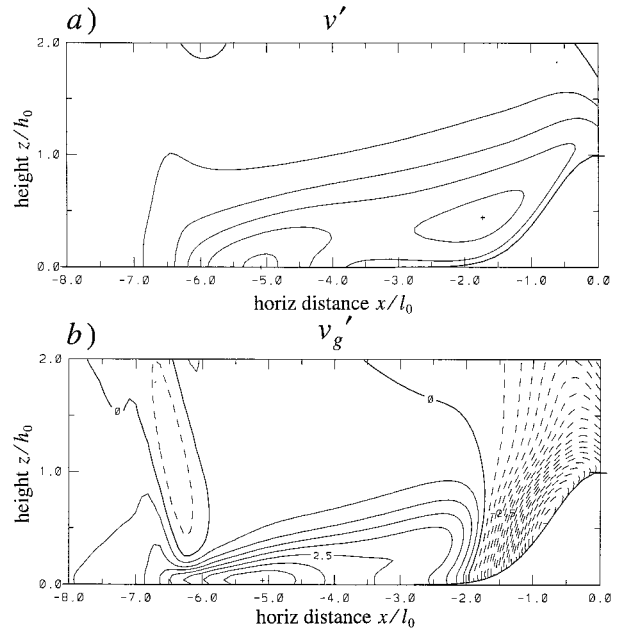

FIG. 12. As Fig. 11 but with surface frictional drag included using $C_D = 0.005$ downstream of $x = -4l_0$.

a reasonable surface wind for New England (Nielsen and Neilley 1990) but rather strong for the deep vertical average across the coast. A large value of u_0 is consistent with Nielsen's (1989) characterization of type-C (orographic) events. Two obvious refinements of the basic model produced unsurprising results: 1) surface frictional drag considerably increases the volume of the blocked air and 2) a long-ridge component of temperature gradient somewhat sharpens the horizontal temperature gradient.

A survey of parameter space for a range of β has quantified the effect of ambient baroclinicity on the minimum mountain height needed for surface flow stagnation. Consistent with the observations, large-scale warm advection, $\beta < 0$, favors stagnation (lowers the Fr threshold), while cold advection inhibits it. There is also a maximum mountain width (Ro^{-1}) for stagnation, and, in the case of strong warm advection ($\beta > -0.5$), a minimum mountain width. The upper bound on the width limits the influence of background rotation. The lower bound (in the case of strong warm advection) keeps the terrain broad enough for the isentropic slope to be significant on the scale of the mountain circulation.

The idealization used here has an environment with unlimited temperature contrast. Based on Xu's (1990) steady-state analysis, this seems to be the main reason why the blocked air does not stop spreading upstream within a reasonable time compared to observations. Xu's analytical model includes vertically varying diffusivity with no-slip conditions at the ground. It shows that a steady density interface is possible for a fixed density contrast and therefore suggests that a time-dependent model might equilibrate if the baroclinicity were confined to a limited area initially.

Even with the model "improvements" in section 3, the horizontal gradients are not as sharp as those observed (e.g., Nielsen and Neilley 1990). This is partly a problem of grid resolution, but may also be due to the omission of diabatic effects, especially latent cooling by melting precipitation in the blocked air (Bell and Bosart 1989) and surface sensible heating over water upstream of the terrain (Bosart 1975). While diabatic processes may be an important detail in reproducing realistic coastal fronts, the present results suggests that they may not always be the primary cause of the frontogenesis.

REFERENCES

Baines, P. G., and P. A. Davies, 1980: Laboratory studies of topographic effects in rotating and/or stratified fluids. *Orographic Effects in Planetary Flows,* GARP Publ. Series, No. 23, WMO/ICSU, 233–299.

Ballentine, R. J., 1980: A numerical investigation of New England coastal frontogenesis. *Mon. Wea. Rev.,* **108,** 1479–1497.

Bell, G. D., and L. F. Bosart, 1989: Large-scale atmospheric structure accompanying New England coastal frontogenesis and associated North American east coast cyclogenesis. *Quart. J. Roy. Meteor. Soc.,* **115,** 1133–1146.

Bennetts, D. A., and B. J. Hoskins, 1979: Conditional symmetric instability: A possible explanation for frontal rainbands. *Quart. J. Roy. Meteor. Soc.,* **105,** 945–962.

Bjerknes, J., and H. Solberg, 1921: Meteorological conditions for the formation of rain. *Geofys. Publ.,* **2,** 10–41.

Blumen, W., 1992: Propagation of fronts and frontogenesis versus frontolysis over orography. *Meteor. Atmos. Phys.,* **48,** 37–50.

——, and B. D. Gross, 1987: Advection of a passive scalar over a finite-amplitude ridge in a stratified rotating atmosphere. *J. Atmos. Sci.,* **44,** 1696–1705.

Bosart, L. F., 1975: New England coastal frontogenesis. *Quart. J. Roy. Meteor. Soc.,* **101,** 957–978.

——, 1984: Texas coastal rainstorm of 17–21 September 1979: An example of synoptic–mesoscale interaction. *Mon. Wea. Rev.,* **112,** 1108–1133.

——, C. J. Vaudo, and J.H. Helsdon Jr., 1972: Coastal frontogenesis. *J. Appl. Meteor.,* **11,** 1236–1258.

Chen, C., J. W. Rottman, and S. E. Koch, 1994: Numerical simulations of upstream blocking, columnar disturbances, and bores in stably stratified shear flows over an obstacle. *Mon. Wea. Rev.,* **122,** 2506–2529.

Davies, P. A., 1984: On the orographic retardation of a cold front. *Beitr. Phys. Atmos.,* **57,** 409–418.

Doyle, J. D., and T. T. Warner, 1993: A numerical investigation of coastal frontogenesis and mesoscale cyclogenesis during GALE IOP 2. *Mon. Wea. Rev.,* **121,** 1048–1077.

Durran, D. R., 1986: Another look at downslope windstorms. Part II: The development of analogs to supercritical flow in an infinitely deep, continuously stratified fluid. *J. Atmos. Sci.,* **43,** 2527–2543.

Egger, J., and H. Hatt, 1994: Passage of a frontal zone over a two-dimensional ridge. *Quart. J. Roy. Meteor. Soc.,* **120,** 557–572.

Garner, S. T., 1986a: An orographic mechanism for rapid frontogenesis. Ph.D. dissertation, Massachusetts Institute of Technology, 222 pp. [Available from MIT, 77 Massachusetts Ave., Cambridge, MA 02139-4307.]

——, 1986b: A radiative upper boundary condition adapted for f-plane models. *Mon. Wea. Rev.,* **114,** 1570–1577.

——, 1995: Permanent and transient upstream effects in nonlinear stratified flow over a ridge. *J. Atmos. Sci.,* **52,** 227–246.

——, 1999: Blocking and frontogenesis by two-dimensional terrain in baroclinic flow. Part II: Analysis of flow stagnation mechanisms. *J. Atmos. Sci.,* **56,** 1509–1523.

Gross, B. D., 1994: Frontal interaction with orography. *J. Atmos. Sci.,* **51,** 1480–1496.

Haderlein, K., 1989: On the dynamics of orographically retarded cold fronts. *Beitr. Phys. Atmos.,* **62,** 11–19.

Huang, C.-Y., 1993: Numerical modeling of topographic influences on shallow front formation and evolution: Quasi-stationary coastal front. *Terr. Atmos. Oceanic Sci.,* **4,** 201–216.

——, and S. Raman, 1992: A three-dimensional numerical investigation of a Carolina coastal front and the Gulf Stream rainband. *J. Atmos. Sci.,* **49,** 560–584.

Kim, Y.-J., S. K. Kar, and A. Arakawa, 1993: A nonreflecting upper boundary condition for anelastic nonhydrostatic mesoscale gravity-wave models. *Mon. Wea. Rev.,* **121,** 1249–1261.

Klemp, J. B., and D. R. Durran, 1983: An upper boundary condition permitting internal gravity wave radiation in numerical mesoscale models. *Mon. Wea. Rev.,* **111,** 430–444.

Kurihara, Y., 1965: On the use of implicit and iterative methods for the time integration of the wave equation. *Mon. Wea. Rev.,* **93,** 33–46.

Lapenta, W. M., and N. L. Seaman, 1990: A numerical investigation of east coast cyclogenesis during the cold-air damming event of 27–28 February 1982. Part I: Dynamic and thermodynamic structure. *Mon. Wea. Rev.,* **118,** 2668–2695.

Long, R. R., 1955: Some aspects of the flow of stratified fluids, III. Continuous density gradient. *Tellus,* **7,** 341–357.

——, 1972: Finite amplitude disturbances in the flow of inviscid rotating and stratified fluids over obstacles. *Annu. Rev. Fluid Mech.,* **4,** 69–92.

McCarthy, D. H., 1977: A study of the vertical structure of the New England coastal front. M.S. thesis, Dept. of Meteorology, University of Wisconsin—Madison, 82 pp. [Available from University of Wisconsin—Madison, 750 University Ave., Madison, WI 53706.]

McIntyre, M. E., 1972: On Long's hypothesis of no upstream influence in uniformly stratified or rotating flow. *J. Fluid Mech.,* **52,** 209–243.

Nielsen, J. W., 1989: The formation of New England coastal fronts. *Mon. Wea. Rev.,* **117,** 1380–1481.

——, and P. P. Neilley, 1990: The vertical structure of New England coastal fronts. *Mon. Wea. Rev.,* **118,** 1794–1807.

Okland, H., 1990: The dynamics of coastal troughs and coastal fronts. *Tellus,* **42A,** 444–462.

Orlanski, I., 1976: A simple boundary condition for unbounded hyperbolic flows. *J. Comput. Phys.,* **21,** 251–269.

Pierrehumbert, R. T., 1985: Stratified semi-geostrophic flow over two-dimensional topography in an unbounded atmosphere. *J. Atmos. Sci.,* **42,** 523–526.

——, and B. Wyman, 1985: Upstream effects of mesoscale mountains. *J. Atmos. Sci.,* **42,** 977–1003.

Raymond, W. H., and H. L. Kuo, 1984: A radiation condition for multi-dimensional flows. *Quart. J. Roy. Meteor. Soc.,* **110,** 535–551.

Schumann, U., 1987: Influence of mesoscale orography on idealized cold fronts. *J. Atmos. Sci.,* **44,** 3423–3441.

Smith, R. B., 1985: On severe downslope winds. *J. Atmos. Sci.,* **42,** 2597–2603.

Williams, R. T., M. S. Peng, and D. A. Zankofski, 1992: Effects of topography on fronts. *J. Atmos. Sci.,* **49,** 287–305.

Xu, Q., 1990: A theoretical study of cold air damming. *J. Atmos. Sci.,* **47,** 2969–2985.

Zehnder, J. A., and P. R. Bannon, 1988: Frontogenesis over a mountain ridge. *J. Atmos. Sci.,* **45,** 628–644.